CONFERENCE PRE-PRINT

GLOBAL ELECTROMAGNETIC SYMMETRY-BREAKING EFFECTS ON MOMENTUM TRANSPORT AND CURRENT GENERATION IN TOKAMAKS

Z.X. Lu, G. Meng, C. Angioni, E. Fable, Ph. Lauber, R. McDermott, M. Hoelzl, ASDEX Upgrade Team Max Planck Institute for Plasma Physics, 85748 Garching, Germany Email: zhixin.lu@ipp.mpg.de

H.Y. Lyu, H.S. Cai

University of Science and Technology of China, Hefei, China

Y Chen

University of Colorado at Boulder, Boulder, United States

F. Zonca

Center for Nonlinear Plasma Science; C.R. ENEA Frascati, Frascati, Italy

Abstract

In the global gyrokinetic solution, symmetry breaking leads to the generation of plasma current and intrinsic ion rotation. This paper introduces the global gyrokinetic code TRIMEG and examines the electromagnetic (EM) effects on the current generation and the parallel momentum transport in tokamak plasmas, taking into account global symmetry-breaking mechanisms such as equilibrium profile variation, linear global mode structure, and nonlinear evolution. The results demonstrate that magnetic effects contribute significantly to current generation, underscoring the importance of an electromagnetic model in predicting turbulence-driven currents. In addition to the fine-structure current reported previously, a large-scale current is also observed. With respect to ion momentum transport, the equilibrium profile is shown to affect both the magnitude and the shape of the ion rotation. Global nonlinear electromagnetic gyrokinetic simulations are applied to predict the intrinsic toroidal rotation profiles of an ASDEX Upgrade (AUG) H-mode plasma with ECRH only. A nonlinear simulation based on AUG experimental profiles, with reduced normalized device size, directly produces an intrinsically generated parallel velocity profile. The simulated velocity profile attains a magnitude comparable to the experimental measurement in the region where the instability is excited.

1. INTRODUCTION

Symmetry breaking in the global gyrokinetic solution modifies the plasma current density profile and plays a critical role in the development of intrinsic ion rotation [1, 2, 3]. Current generation in turn influences the MHD equilibrium and associated instabilities. Plasma rotation can suppress microinstabilities and prevent MHD mode locking, thereby improving confinement and stability. In ITER, the external torque from neutral beam injection (NBI) is expected to be insufficient to drive strong toroidal rotation, making intrinsic sources of rotation particularly important. Similarly, current DEMO designs and the early operational phase of ITER will largely rely on intrinsic rotation in the absence of NBI. Most previous studies of intrinsic rotation have been carried out in the electrostatic limit, neglecting electromagnetic effects.

The turbulence-driven current has been investigated theoretically [4, 5, 6]. Previous gyrokinetic simulations of intrinsic rotation have primarily relied on electrostatic models and thus focused on electrostatic modes such as the ion temperature gradient mode (ITG) and the trapped electron mode (TEM) [7, 8, 9]. For electron momentum transport (current generation), gyrokinetic simulations have identified both large-scale and fine-scale structures in the radial current profile, indicating that turbulence-driven current is not negligible compared with the bootstrap current [10, 11, 12]. Moreover, the magnetic contribution to the parallel momentum flux can be significant even for ion-temperature-gradient modes [13]. In the symmetry breaking studies related to energetic particles, the electromagnetic effect is the starting point of the simulations of Alfvèn eigenmodes [14, 15].

In this work, the electromagnetic gyrokinetic code TRIMEG is employed to simulate ion rotation and current generation. Section 2 describes the models and equations used in TRIMEG, Section 3 presents the simulation results for current generation and ion rotation, and Section 4 provides the conclusions.

2. MODELS AND EQUATIONS

2.1. The gyrokinetic electromagnetic model in TRIMEG code

The TRIangular MEsh-based Gyrokinetic code (TRIMEG) has been originally based on unstructured triangular meshes and C^0 linear finite elements [16]. It has been extended to the high-order C^1 finite element method in triangular meshes recently [17]. Meanwhile, the structured mesh version has also been developed for studies of numerical methods such as the implicit scheme [18], the piecewise field-aligned finite element method [19], and physics models such as the mixed-full f- δf method for energetic particle and Alfvénic physics [20]. The recent studies of Alfvén waves and micro-instabilities using TRIMEG-GKX has been summarized previously [21]. In this work, we use the structured mesh version TRIMEG-GKX to study the momentum transport of the electrons and ions. Specifically, the mixed variable-pullback scheme has been adopted, which is crucial for electromagnetic simulations in this work.

Using the mixed variable scheme, the parallel component of the perturbed magnetic potential δA_{\parallel} is decomposed into a symplectic part $\delta A_{\parallel}^{\rm s}$ and a Hamiltonian part $\delta A_{\parallel}^{\rm h}$ [22], namely, $\delta A_{\parallel} = \delta A_{\parallel}^{\rm s} + \delta A_{\parallel}^{\rm h}$. The gyrocenter equations of motion are as follows [22, 23, 24, 25, 26],

$$\dot{\boldsymbol{R}}_{0} = u_{\parallel} \boldsymbol{b}_{0}^{*} + \frac{m\mu}{qB_{\parallel}^{*}} \boldsymbol{b} \times \nabla B , \quad \dot{u}_{\parallel,0} = -\mu \boldsymbol{b}_{0}^{*} \cdot \nabla B , \qquad (1)$$

$$\delta \dot{\boldsymbol{R}} = \frac{\boldsymbol{b}}{B_{\parallel}^*} \times \nabla \langle \delta \Phi - u_{\parallel} \delta A_{\parallel} \rangle - \frac{q_s}{m_s} \langle \delta A_{\parallel}^{\text{h}} \rangle \boldsymbol{b}^* , \qquad (2)$$

$$\delta \dot{u}_{\parallel} = -\frac{q_s}{m_s} \left(\boldsymbol{b}^* \cdot \nabla \langle \delta \Phi - u_{\parallel} \delta A_{\parallel}^{\rm h} \rangle + \partial_t \langle \delta A_{\parallel}^{\rm s} \rangle \right) - \frac{\mu}{B_{\parallel}^*} \boldsymbol{b} \times \nabla B \cdot \nabla \langle \delta A_{\parallel}^{\rm s} \rangle , \qquad (3)$$

where $u_{\parallel} = v_{\parallel} + (q_s/m_s)\langle \delta A_{\parallel}^{\rm h} \rangle$, v_{\parallel} is the parallel velocity, q_s and m_s are the charge and mass of species s, respectively, the subscript "s" represents the different particle species (in the following, thermal ions and electrons are kept), and $\langle \ldots \rangle$ indicates the gyro average, $\delta \Phi$ is the perturbed electrical potential, the magnetic moment $\mu = v_{\perp}^2/(2B)$, $\boldsymbol{b}^* = \boldsymbol{b}_0^* + \nabla \langle \delta A_{\parallel}^{\rm s} \rangle \times \boldsymbol{b}/B_{\parallel}^*$, $\langle \ldots \rangle$ denotes the gyro average, $\boldsymbol{b}_0^* = \boldsymbol{b} + (m_s/q_s)u_{\parallel}\nabla \times \boldsymbol{b}/B_{\parallel}^*$, $\boldsymbol{b} = \boldsymbol{B}/B$, $B_{\parallel}^* = B + (m_s/q_s)u_{\parallel}\boldsymbol{b} \cdot (\nabla \times \boldsymbol{b})$, \boldsymbol{B} is the equilibrium magnetic field.

The perturbed distribution function is solved by following the marker trajectory.

$$\frac{\mathrm{d}\delta f}{\mathrm{d}t} = \frac{\partial}{\partial t}\delta f + \dot{\mathbf{R}} \cdot \nabla \delta f + \dot{u}_{\parallel} \frac{\partial}{\partial \dot{u}_{\parallel}} \delta f = -\delta \dot{\mathbf{R}} \cdot \nabla f_0 - \delta \dot{u}_{\parallel} \frac{\partial}{\partial u_{\parallel}} f_0 , \qquad (4)$$

where $\dot{\mathbf{R}} = \dot{\mathbf{R}}_0 + \delta \dot{\mathbf{R}}$, $\dot{u}_{\parallel} = \dot{u}_{\parallel,0} + \delta \dot{u}_{\parallel}$, the equilibrium distribution f_0 is the steady state solution that satisfies $\mathrm{d}f_0/\mathrm{d}t|_0 = 0$ along the unperturbed trajectory, and it is typically assumed to be the Maxwellian distribution function when the neoclassical physics is not considered in toroidally confined plasmas.

The linearized quasi-neutrality equation with the long-wavelength approximation is as follows,

$$-\nabla \cdot (G\nabla_{\perp}\delta\Phi) = \sum_{s} q_{s}\delta n_{s,v} \equiv \delta Q_{v} , G = \sum_{s} \frac{q_{s}n_{0s}}{B\omega_{cs}}$$
 (5)

where the gyrocenter density $\delta n_{s,v}$ is calculated using $\delta f_s({\pmb R},v_\parallel,\mu)$ (denoted as $\delta f_{s,v}$), namely, $\delta n_{s,v}({\pmb x})=\int {\rm d}^6z\,\delta f_{s,v}\delta({\pmb R}+{\pmb \rho}-{\pmb x})$. Here, ${\pmb x}$ and ${\pmb R}$ denote the particle position vector and gyrocenter position vector, respectively, and ${\pmb \rho}$ represents the Larmor radius vector. In Eq. (5), $\omega_{\rm cs}$ is the cyclotron frequency of species s. $\delta f_{s,v}$ is obtained from $\delta f_{s,u}$ according to the general form of the nonlinear pullback scheme [23] $f_{s,v}(v_\parallel)=f_{s,u}(v_\parallel+(q_s/m_s)\langle\delta A_\parallel^h\rangle)$.

Ampère's law

$$-\nabla_{\perp}^{2} \delta A_{\parallel} = \mu_{0} \sum_{s} q_{s} \int d^{6}z \, v_{\parallel} \delta f_{s,v} \delta(\boldsymbol{R} + \boldsymbol{\rho} - \boldsymbol{x}) \equiv \delta j_{v}$$
 (6)

is expressed as

$$-\nabla_{\perp}^{2} \delta A_{\parallel}^{h} + \sum_{s} \mu_{0} \frac{q_{s}^{2}}{T_{s}} \int d^{6}z \, v_{\parallel}^{2} f_{0s} \langle \delta A_{\parallel}^{h} \rangle \delta(\mathbf{R} + \boldsymbol{\rho} - \boldsymbol{x})$$

$$= \nabla_{\perp}^{2} \delta A_{\parallel}^{s} + \mu_{0} \sum_{s} q_{s} \int d^{6}z \, v_{\parallel} \delta f_{s,u}(u_{\parallel}) \delta(\mathbf{R} + \boldsymbol{\rho} - \boldsymbol{x}) . \tag{7}$$

The ideal Ohm's law is adopted to determine $\delta A_{\parallel}^{\rm s}$,

$$\partial_t \delta A^{\rm s}_{\parallel} + \partial_{\parallel} \delta \Phi = 0 \quad , \tag{8}$$

where the parallel derivative is defined as $\partial_{\parallel} = \mathbf{b} \cdot \nabla$, $\mathbf{b} = \mathbf{B}/B$ as already defined following Eq. (3). At the end of each step, the solution is pulled back from $(\delta f_{s,u}, u_{\parallel})$ to $(\delta f_{s,v}, v_{\parallel})$,

$$\delta f_{s,u}^{\text{new}} = \delta f_{s,u}^{\text{old}} + \frac{q_s \left\langle \delta A_{\parallel}^{\text{h,old}} \right\rangle}{m_s} \frac{\partial f_{0s}}{\partial v_{\parallel}} \xrightarrow{\text{Maxwellian}} \delta f_{s,u}^{\text{old}} - \frac{v_{\parallel}}{T_s} q_s \left\langle \delta A_{\parallel}^{\text{h,old}} \right\rangle f_{0s} , \qquad (9)$$

$$u_{\parallel}^{\text{new}} = u_{\parallel}^{\text{old}} - \frac{q_s}{m_s} \left\langle \delta A_{\parallel}^{\text{h,old}} \right\rangle , \quad \delta A_{\parallel}^{\text{s,new}} = \delta A_{\parallel}^{\text{s,old}} + \delta A_{\parallel}^{\text{h,old}} , \quad \delta A_{\parallel}^{\text{h,new}} = 0 . \qquad (10)$$

$$u_{\parallel}^{\text{new}} = u_{\parallel}^{\text{old}} - \frac{q_s}{m_s} \langle \delta A_{\parallel}^{\text{h,old}} \rangle , \quad \delta A_{\parallel}^{\text{s,new}} = \delta A_{\parallel}^{\text{s,old}} + \delta A_{\parallel}^{\text{h,old}} , \quad \delta A_{\parallel}^{\text{h,new}} = 0 .$$
 (10)

A 4th-order Runge-Kutta time integrator is implemented in the TRIMEG code, and the pullback operation is applied at the end of each full time step.

2.2. The diagnoses of the parallel momentum fluxes

The flux diagnostics of particle, heat, and parallel momentum have been implemented for all particle species, including both electrons and ions. Specifically, the parallel momentum, the fluxes due to the scalar potential, and the parallel component of the vector potential are separated as follows

$$\Pi_{\delta\phi} = \left\langle \int d^3 v \frac{\mathbf{b}}{B} \times \langle \nabla \delta \phi \rangle \delta f_v v_{\parallel} \right\rangle_F , \quad \Pi_{\delta A_{\parallel}} = \left\langle \int d^3 v \frac{\mathbf{b}}{B} \times \langle \nabla \delta A_{\parallel} \rangle \delta f_v v_{\parallel}^2 \right\rangle_F , \tag{11}$$

where δf_v is the perturbed distribution in $(\mathbf{R}, v_{\parallel}, \mu), \langle \cdots \rangle$ denotes the gyro-average and $\langle \ldots \rangle_F$ denotes the flux surface average. The current and the parallel velocity are calculated as follows,

$$\delta j_{\parallel,e} = -e \left\langle \int d^3 v \delta f_{v,e} v_{\parallel} \right\rangle_F , \quad V_{\parallel} = \left\langle \frac{1}{n_i} \int d^3 v \delta f_{v,i} v_{\parallel} \right\rangle_F , \quad (12)$$

where n_i is the ion density. Since the perturbed distribution function is pulled back to v_{\parallel} space at the end of each step in Eq. (9), δf_v is always close to δf_u and $\delta f_v = \delta f_u$ after pullback. The flux contributions from the electrostatic scalar potential and the parallel component of the vector potential are analyzed separately to quantify their respective roles. Note that while the contribution from $\delta \phi$ and δA_{\parallel} is separated as shown in Eq. (11), the perturbed distribution implicitly depends on $\delta\phi$ and δA_{\parallel} and can not be explicitly separated from the results.

3. RESULTS AND ANALYSES

We perform single-n and multi-n simulations. The Maxwellian distribution markers are initially loaded, and δf is initialized with noise. The evolution of the distribution function $f = f_0 + \delta f$ is represented by the perturbed part δf while the analytical expression of f_0 does not change in the simulation. In both single-n and multi-n simulations, the n=0 component in phase space is free to evolve, and thus, even in the single-n simulations, the profile flattening can occur to saturate the instability.

3.1. Current generation in the Cyclone-like case

3.1.1. Parameters

We consider an ad hoc equilibrium with circular magnetic surfaces, similar to that used in the previous gyrokinetic simulations [11, 13]. The parameters are similar to those of the Cyclone base case with $a/R_0 = 0.36$, $R_0 =$ 1.67 m. The plasma temperature is tuned to study the cases with different orbit width by shifting the normalized device size $a/\rho_{\rm ref}$, where $\rho_{\rm ref}=m_N v_N/(eB_{\rm ref})$ is the reference Larmor radius using the proton mass m_N , the velocity unit $v_N = \sqrt{2T_{\rm ref}/m_N}$, the temperature unit $T_{\rm ref}$ is determined by $\rho_{\rm ref}$ and $\beta_{\rm ref}$ (defined later), and $B_{\rm ref}=2$ T. For the economical Cyclone case, we choose $\rho_{\rm ref}=0.0066844$ m, and thus the ratio $a/\rho_{\rm ref}\approx90$ (the nominal value is 180). In addition to $\rho_{\rm ref}$, we choose another parameter $\beta_{\rm ref} = \mu_0 n_{\rm ref} m_N v_N^2 / B_{\rm ref}^2$ so that $n_{\rm ref}$ and $T_{\rm ref}$ are determined, and $n_{\rm ref}$ and $T_{\rm ref}$ correspond to the values at the reference radius. The details of the normalization can be found in our previous work [20]. The mass ratio is $m_i/m_e = 100$. Our future work will focus on more realistic simulations, whereas this work concentrates on studying the basic properties while considering electromagnetic effects. Two cases with $\beta_{\rm ref}=0.005, 0.02$ are simulated with the n=10 Fourier filter in the field solver. The ITG mode and KBM are dominant for $\beta_{\rm ref}=0.005,0.02$, respectively. Figure 1 demonstrates the time evolution of the total field energy that is estimated as $E_{\rm field} = -\int {\rm d}V (\delta\phi\delta Q_v + \delta A_{\parallel}\delta j_v)$ where δQ_v and δj_v are defined in Eqs. (5) and (6). The parallel momentum and the fluxes are calculated using the data in the nonlinear stage with time average and analyzed in the following section.

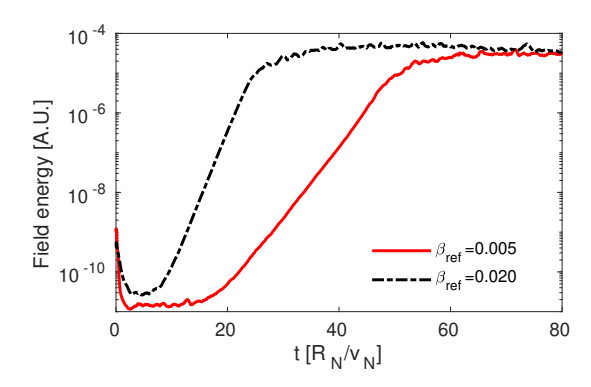


FIG. 1. The time evolution of the total field energy for $\beta_{ref} = 0.005, 0.02, n = 10.$

3.1.2. Structures of the perturbed density and current

The nonlinear simulations have been performed for the n=10 toroidal harmonic. Typical 2D structures of the perturbed density and current are shown in Fig. 2 for $\beta_{\rm ref}=0.005$. The tilting of the 2D mode structure is visible, indicating the symmetry-breaking effect on the momentum transport [2, 27, 28]. In the linear stage, the nonlinear terms are negligible, and the instability grows exponentially. Once the mode amplitude exceeds a critical threshold, nonlinear effects become significant, driving the instability into its nonlinear stage, where it saturates due to the $E \times B$ and parallel nonlinear terms. Specifically, in the single-n simulations, we only apply the toroidal Fourier filter when solving the field variables $\delta\phi$ and δA_{\parallel} , but the n=0 component can still evolve. The so-called $E \times B$ nonlinearity $\delta \mathbf{v} \cdot \nabla \delta f$ and the parallel nonlinearity $\delta \psi_{\parallel} \partial \delta f / \partial v_{\parallel}$ in Eq. (4) can balance the radial gradient of f_0 and lead to the saturation of the instability. Since these are single-n simulations, the mode structure is coherent even in the nonlinear stage. From the linear stage to the nonlinear stage, the mode structure is broadened while the tilting angle remains finite. The right frame demonstrated that the radial widths of the density perturbation and the current perturbation is larger in the nonlinear stage than in the linear stage. In the radial profile of the density perturbation, the fine structures are also significant. Note that the zonal component is not included. Thus, the shearing effect of the zonal flow is not included since the purpose is merely to identify the properties of the current driven by the single-n harmonic.

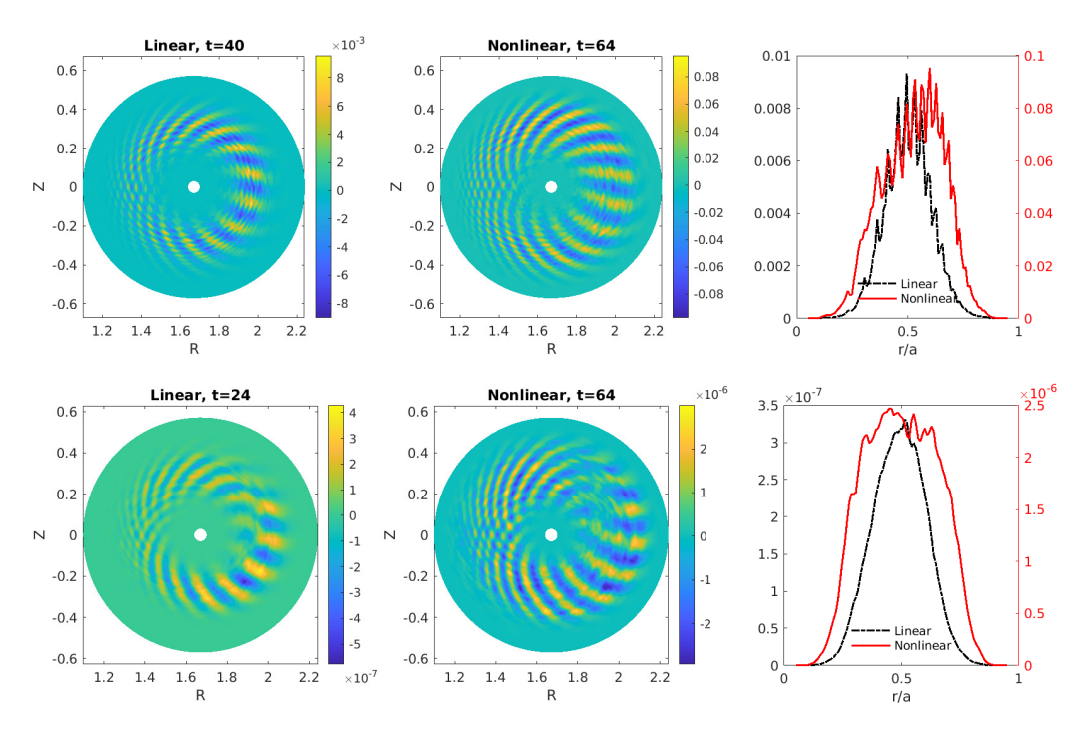


FIG. 2. The structure of the perturbed density (upper) and current (lower) for $\beta_{\rm ref}=0.005$, n=10. The right column is the radial profile calculated at $\phi=0$ according to $\bar{Y}(r_i)\equiv\sqrt{\sum_{j=1,N_\theta}Y^2(r_i,\theta_j)/N_\theta}$, where N_θ is the poloidal grid number.

3.1.3. Multi-scale turbulence-driven current

The large-scale and fine-scale of the turbulence-driven current have been reported previously in the electrostatic limit or low β plasma [12, 10, 13]. Without including the n=0 component, the ITG/TEM instability is saturated due to the $E\times B$ nonlinearity $\delta \mathbf{v}\cdot\nabla\delta f$ and the parallel nonlinearity $\delta\dot{v}_{\parallel}\partial\delta f/\partial v_{\parallel}$ in Eq. (4) that locally flattens the instability drive (the temperature and/or density gradient in the radial direction). Meanwhile, since the Fourier filter is applied only when calculating the perturbed density and current for solving the quasi-neutrality equation and the parallel Ampère's law, the evolution of $\delta n_{n=0}$ and $\delta j_{n=0}$ is not suppressed and can be viewed as a quasi-linear estimate. While the accurate magnitude relies on a more consistent simulation, the single-n simulation can be used to identify the multi-scale structures. The n=0, m=0 component of the turbulence-driven current is shown in Fig. 3. The fine structure of $\delta j_{n=0,m=0}$ is demonstrated by the red solid lines. By applying smoothing with a radial span of $\sim 0.17a$, the large-scale structure of the current is obtained, as indicated by the black dashed line. The $\beta_{\rm ref}=0.02$ case is also simulated in the right frame. The two-scale structure shows differences from that of the $\beta_{\rm ref}=0.005$ case, since the negative large-scale current also appears in the inner region, which can be related to the different dependence of symmetry breaking on various parameters and the mode type.

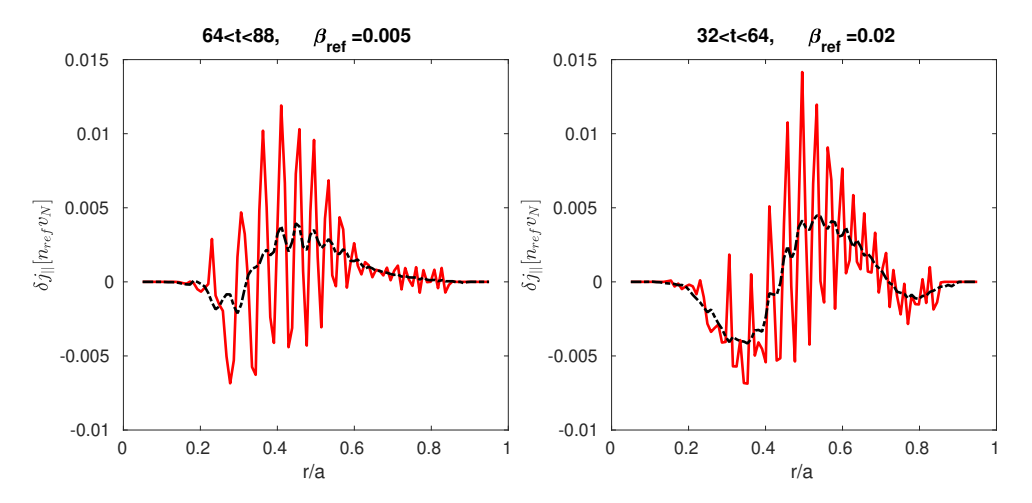


FIG. 3. The radial structure of the turbulence driven n=0, m=0 current for $\beta_{ref}=0.005$ (left) and $\beta_{ref}=0.02$ (right).

3.1.4. Electromagnetic effects

The parallel momentum flux is calculated according to Eqs. (11) and normalized to the Gyro Bohm scaling. As shown in Fig. 4, for $\beta_{\rm ref}=0.005$, the electron parallel momentum flux is mainly contributed by $\Pi_{\delta\phi}$. For the $\beta_{\rm ref}=0.02$ case, the magnitude of $\Pi_{\delta A}$ increases and is similar to that of $\Pi_{\delta\phi}$ near r/a=0.4, suggesting that the electromagnetic effect is important for evaluating the electron parallel momentum flux.

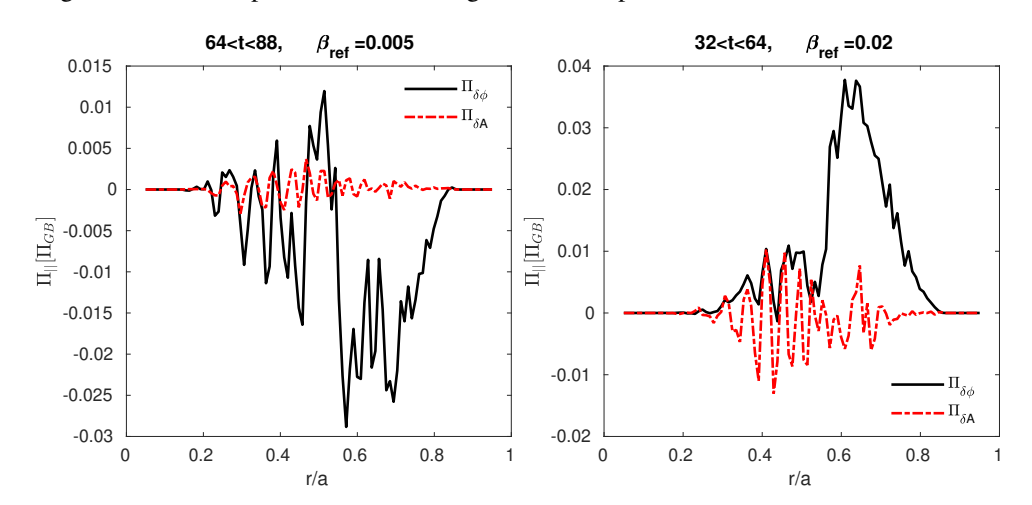
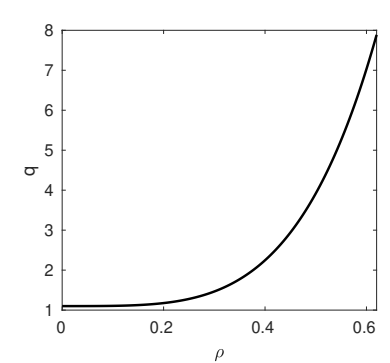


FIG. 4. The radial structure of the electron parallel momentum flux (Eq. 11) for $\beta_{ref} = 0.005$ (left) and $\beta_{ref} = 0.02$ (right).

3.2. Parallel rotation generation in the AUG-like case

3.2.1. Parameters

The simulation of ion rotation is based on the parameters of the AUG discharge # 26170 at \sim 3.86 s [3]. It is an H-mode, with about 2.2 MW of ECRH heating power, at 2.5 T and 0.6 MA. The ad hoc equilibrium with concentric circular flux surfaces is adopted with $R_0=1.7$ m, a=0.62 m, $B_{\rm ref}=2.5$ T. The safety $q(\rho)$ is matched to the experimental profile $\bar{q}(\rho)=q_0+q_4\rho^4$, where $q_0=1.1$, $q_2=0$, $q_4=48.0498$, $\rho=\sqrt{(R-R_0)^2+(Z-Z_0)^2}$, $\rho\in[0,a]$ and in the ad hoc equilibrium model, $q(\rho)=\bar{q}/\sqrt{1-(\rho/R_0)^2}$. The density and temperature profiles are from the experimental measurement, as shown in Fig. 5. While our ultimate goal is to consider realistic parameters, in this work, we choose $\rho_{\rm ref}=0.0066844$ m instead of the nominal value $\rho_{\rm ref}=0.0018278$ m due to the limitation on computational resources. From our previous numerical studies, the computational cost is proportional to $1/\rho_{\rm ref}^3$ (Eq. 97 in [29]) and thus, the increased $\rho_{\rm ref}$ reduces the computational cost significantly to make it affordable. In addition, as $\rho_{\rm ref}$ decreases, the n spectrum shifts upward and the net flux decreases, requiring longer-time simulations. The electrostatic model is adopted since the electromagnetic effect is expected to play a minor role in ion rotation. Nevertheless, the following studies aim to demonstrate the basic properties of the simulation and a more accurate evaluation using realistic parameters merits more effort in the future.



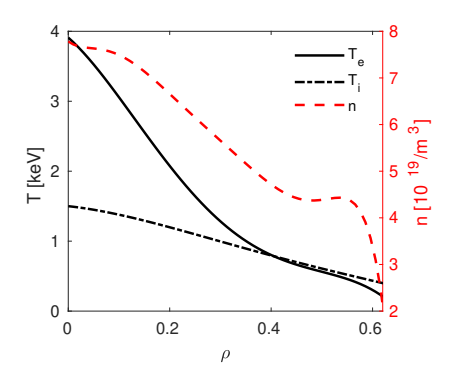


FIG. 5. The radial profile of the safety factor (left) and temperature and density (right) of the AUG case.

3.2.2. Multi-n nonlinear simulations

The time evolution of the total field energy is shown in the upper frame of Fig. 6. The piecewise field-aligned finite element method has been used to reduce the grid number in the direction along the magnetic field [19]. No Fourier filter has been applied in the simulation. The most unstable mode appears from the noise and becomes dominant in the linear stage. The time evolution of the total field energy (top left) exhibits the exponential growth of the instability followed by its saturation. The 2D structures of the density perturbation are shown in the lower frame. The linear mode structure (lower left) is much narrower than that in the nonlinear stage (lower right). While the 2D mode structure in the nonliner stage is not turbulent enough, due to the increased $\rho_{\rm ref}/a$ in this simulation, the broadening of the mode structure in the radial direction is observed (top right). More detailed studies related to the turbulence spreading relies on more realistic simulation using small $\rho_{\rm ref}/a$ and dedicated analyses of the zonal flow in future, with necessary comparison with previous work [30].

3.2.3. Profile generation of toroidal rotation

Previous work solves a transport equation by extracting the predicted momentum flux from the gyrokinetic simulation [30]. Electrostatic global simulations analyzed the symmetry breaking mechanisms and the rotation profile generation for AUG [31]. In this work, the flow profile is simulated directly by the nonlinear gyrokinetic simulation and compared with the experimental measurements. The general feature of a hollow rotation profile observed in ASDEX Upgrade (ECRH H-modes) is reproduced by nonlinear simulations. The multi-nonlinear simulation is run with global effects such as self-consistent background profile variation represented by δf including its n=0, m=0 component.

The evolution of the ion parallel momentum flux is shown in Fig. 7 (left), where the radial broadening of structure is visible from the linear to the nonlinear stage. The generation of the rotation profile is closely linked to turbulence broadening in the radial direction, since the rotation profile varies across the entire radial domain from the experimental observation but the linear mode structure mainly accumulates near $r/a \sim 0.4$. From the ion toroidal angular momentum transport equation, $\partial_t(m_i n_i \langle RV_\phi \rangle_F) + \langle \nabla \cdot \Gamma_\phi \rangle_F = S$, where Γ_ϕ is the total toroidal

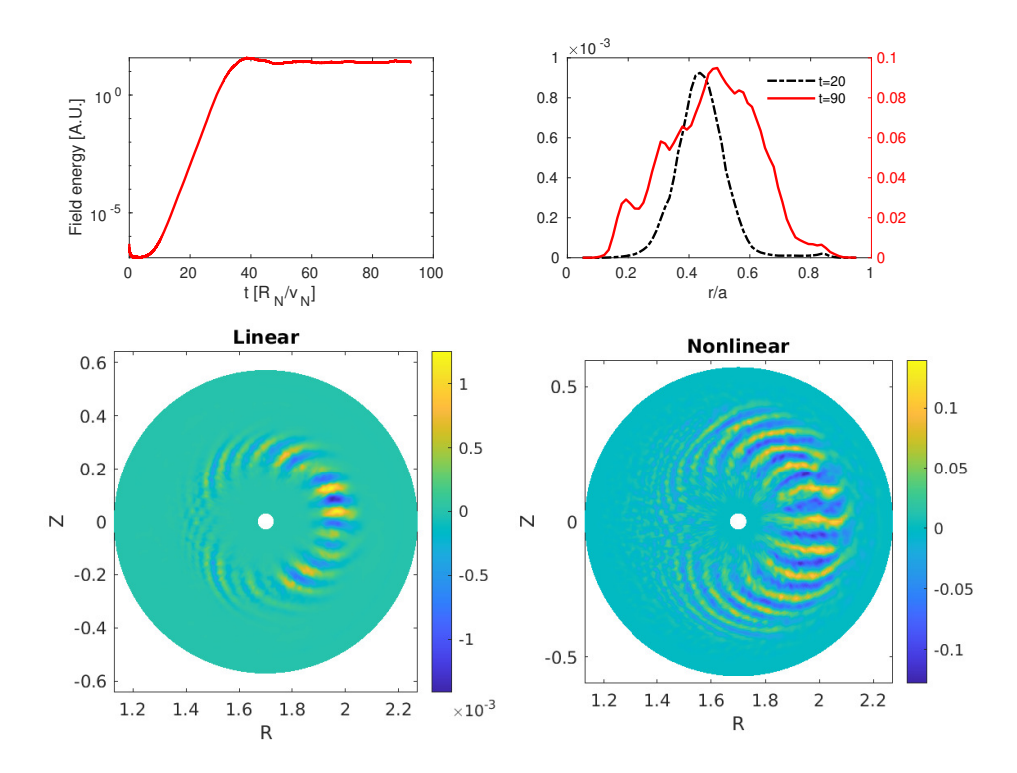


FIG. 6. The time evolution of the total field energy (upper left), the radial structure (top right) and the 2D structures (lower) of the density perturbation at $t=(20,90)R_{\rm N}/v_{\rm N}$ for the AUG case. The radial structure is calculated with the same way as Fig. 2. The unit of $\delta\Phi$ is $m_{\rm N}v_{\rm N}^2/e=2$ kV. At saturation, $\delta\Phi\sim0.05$, corresponding to ~100 V. Simulations with smaller $\rho_{\rm ref}/a$ are expected to yield lower magnitude of $\delta\Phi$.

angular momentum flux and mainly contributed by the the parallel ion momentum flux, and S is the momentum source such as that arising from neutral beam injection, which is set to zero in simulations. In the middle frame, near the axis, the positive $\langle \nabla \cdot \Gamma_{\phi} \rangle_F$ corresponds to a negative parallel velocity; while in the outer region, vice versa. The parallel velocity does not keep increasing in the nonlinear stage since other mechanisms such as the turbulent diffusion can balance the residual stress. The parallel velocity is calculated in the nonlinear stage by time-average during $t \in [60,70]R_{\rm N}/v_{\rm N}$ as shown in Fig. 7 (right). In the region where the instability is strong $(0.2 \ll r/a \ll 0.6)$, the simulation result follows the trend of the experimental measurement, while near the inner and outer boundary, more realistic simulations are needed, taking into account more realistic ρ^* values and advanced boundary treatment.

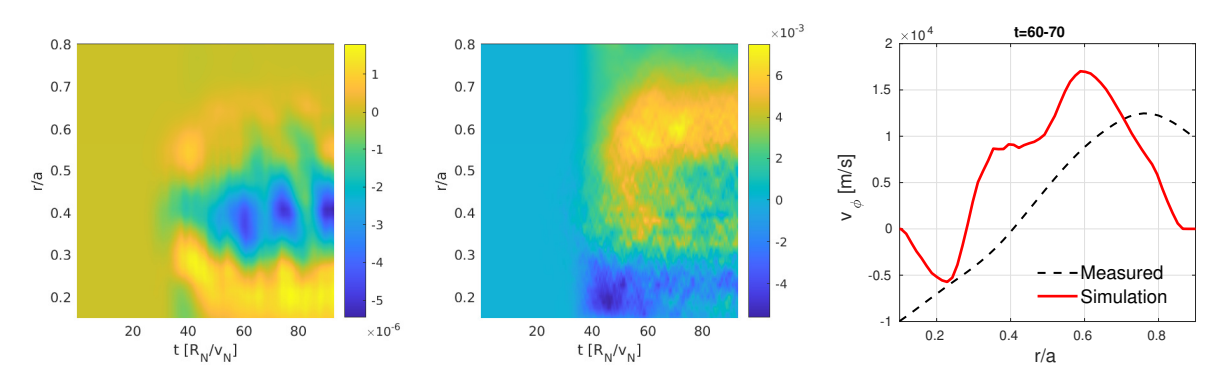


FIG. 7. The parallel ion momentum flux (left), the parallel velocity (middle) and radial profile of the rotation from the simulation and the experimental measurement (right) of the AUG case.

4. SUMMARY

The new electromagnetic global gyrokinetic code TRIMEG enables the study of turbulence-driven ion momentum transport and current generation on an equal footing. For ITG/KBM-driven current, multi-scale structures

are identified. In the high- $\beta(2\%)$ case, the electromagnetic correction in fine-scale flux is significant compared with that driven by the electrostatic scalar potential. The general feature of a hollow ion toroidal rotation profile observed in ECRH H-modes in ASDEX Upgrade has been reproduced by global nonlinear electromagnetic gyrokinetic simulations. This work demonstrates that turbulence can modify the current and rotation profiles, thereby affecting plasma confinement. Future work aims to perform simulations at reactor-relevant values of a/ρ_i . The neoclassical effect with finite collision can be also important and merits more effort in the future.

ACKNOWLEDGEMENTS

The simulations in this work were run on the TOK cluster and the MPCDF Viper/Raven supercomputers. The Eurofusion projects TSVV-8, ACH/MPG and TSVV-10 are acknowledged. This work has been carried out within the framework of the EUROfusion Consortium, funded by the European Union via the Euratom Research and Training Programme (Grant Agreement No 101052200—EUROfusion). Views and opinions expressed are however those of the author(s) only and do not necessarily reflect those of the European Union or the European Commission. Neither the European Union nor the European Commission can be held responsible for them.

REFERENCES

- [1] Ö. D. Gürcan et al. In: *Physics of Plasmas* 14.4 (2007).
- [2] Y. Camenen et al. In: Nuclear Fusion 51.7 (2011), p. 073039.
- [3] C. Angioni et al. In: *Physical Review Letters* 107.21 (2011), p. 215003.
- [4] C. J McDevitt, X-Z Tang, and Z. H. Guo. In: *Physics of Plasmas* 24.8 (2017).
- [5] X. Garbet et al. In: Journal of Physics: Conference Series. Vol. 561. 1. IOP Publishing. 2014, p. 012007.
- [6] F. L. Hinton, R. E. Waltz, and J. Candy. In: *Physics of Plasmas* 11.5 (2004), pp. 2433–2440.
- [7] W.X. Wang et al. In: *Physical Review Letters* 106.8 (2011), p. 085001.
- [8] S. Ku et al. In: *Nuclear Fusion* 52.6 (2012), p. 063013.
- [9] I. Holod and Z. Lin. In: Plasma Physics and Controlled Fusion 52.3 (2010), p. 035002.
- [10] W. X. Wang et al. In: *Nuclear Fusion* 59.8 (2019), p. 084002.
- [11] X. Chen et al. In: *Physics of Plasmas* 28.11 (2021).
- [12] X. Chen et al. In: Plasma Physics and Controlled Fusion 64.11 (2022), p. 115008.
- [13] H. Y. Lyu et al. In: *Physics of Plasmas* 32.5 (2025).
- [14] G. Meng et al. In: Nuclear Fusion 60.5 (2020), p. 056017.
- [15] G. Meng et al. In: *Plasma Science and Technology* 24.2 (2022), p. 025101.
- [16] Z. X. Lu et al. In: *Phys. Plasmas* 26.12 (2019), p. 122503.
- [17] Z. X. Lu et al. In: Journal of Computational Physics (2025), p. 113811.
- [18] Z. X. Lu et al. In: Journal of Computational Physics 440 (2021), p. 110384.
- [19] Z. X. Lu et al. In: Journal of Plasma Physics 91.2 (2025), E48.
- [20] Z. X. Lu et al. In: Plasma Physics and Controlled Fusion (2023).
- [21] Z. X. Lu et al. In: arXiv preprint arXiv:2504.21837 (2025).
- [22] A. Mishchenko et al. In: Physics of Plasmas 21.9 (2014).
- [23] R. Hatzky et al. In: Journal of Plasma Physics 85.1 (2019).
- [24] E. Lanti et al. In: Computer Physics Communications 251 (2020).
- [25] A. Mishchenko et al. In: Journal of Plasma Physics 89.3 (2023), p. 955890304.
- [26] R. Kleiber et al. In: Computer Physics Communications 295 (2024), p. 109013.
- [27] Z. X. Lu. In: *Physics of Plasmas* 22.5 (2015).
- [28] Z. X. Lu et al. In: *Physics of Plasmas* 24.4 (2017).
- [29] Z. X. Lu et al. In: *Plasma Physics and Controlled Fusion* 67.1 (2024), p. 015015.
- [30] W.X. Wang et al. In: *Physics of Plasmas* 24.9 (2017).
- [31] W. A. Hornsby et al. In: *Nuclear Fusion* 58.5 (2018), p. 056008.